Application of infrared thermography to the evaluation of local convective heat transfer on arrays of cubical protrusions

E. R. Meinders,* Th. H. van der Meer,* K. Hanjalić,* and C. J. M. Lasance†
*Delft University of Technology, Applied Physics Department, Delft, The Netherlands, and
†Philips Research, Nederlandse Philips Bedrijven B.V., Eindhoven, The Netherlands

This paper reports on the experimental technique and measurement method used for the investigation of the local convective heat transfer from cubical protrusions placed on a vertical wall of a rectangular-sectioned wind tunnel. This experimental configuration simulates a simplified air-cooled vertical electronic circuit board, resembling a situation in an electronic cabinet. A controlled heat flux was generated by internal heating of the elements. An advanced infrared system was used to measure the surface temperatures of the cubical elements, which is crucial for determining the local convective heat transfer. The difficulties and uncertainties encountered in the course of measurements are discussed together with possible solutions of the problems. A selection of results, validated by means of an uncertainty analysis, is presented, showing a strong variation of the local convective heat transfer around the individual elements. Qualitative interpretation of the local heat transfer coefficients was facilitated by smoke visualization of the mean flow pattern around the protrusions. *© 1997 by Elsevier Science Inc.*

Keywords: 3-D infrared thermography; local convective heat transfer; cubical protrusions; separated and impinging flow

Introduction

The ever-increasing power dissipation in printed circuit boards and the miniaturisation of electronic circuitry impose more and more stringent demands for an efficient thermal management in order to guarantee the reliability of electronic equipment. Despite progress in cooling techniques over the past few decades, local overheating is still one of the major causes of technical failure. Complex configuration of the interior of an electronic cabinet obstructs the coolant flow and generates flow separation and recirculation in some regions. Combined with concentrated heat dissipation within the elements, the complex flow pattern causes high nonuniformity of the convective and radiative heat transfer. Hence, knowledge of the details of the heat transfer mechanisms is essential for the design of an optimum cooling system. A reliable prognosis and avoidance of hot spots and critical temperatures in a variety of complex printed circuit boards is based on a technique that allows for an accurate evaluation of the local heat transfer and temperature on and around the elements (Moffat and Anderson 1990).

This paper reports on the investigation of the local convective heat transfer from a packed array of wall-mounted, heated cubical elements placed on one of the vertical walls in a channel flow. This configuration represents the components of an idealized printed circuit board, cooled by a low-velocity air stream induced by a fan. An adequate calibration procedure, which is required for accurate temperature measurements, is discussed in detail. An advanced infrared system was used to measure three-dimensional (3-D) surface temperatures. The difficulties and uncertainties encountered in the course of measurements are discussed together with possible solutions of the problems.

The results, validated by means of an uncertainty analysis, indicated a strong variation of the local convective heat transfer around the individual elements. These measurements were complemented by studies of flow patterns around the elements using smoke visualisation.

Test configuration and physical model

The experiments were performed in a modified wind-tunnel section. The channel width was 50 mm. The top and bottom walls were 500-mm apart, eliminating any substantial three-dimensional (3-D) effects, at least in the midheight plane. Nine internally heated cubical elements, 15 mm in size, were equidistantly placed in a packed array on one of the vertical walls. The distance between the subsequent elements was 15 mm. The array consisted of seven active (measurement) elements and two additional elements used for calibration, denoted by 7, and location identification (grid element) denoted by 9, all shown in Figure 1. Only the first six elements (1–6) were used to measure the convective heat transfer. The measurement element between the grid and calibration element was used to establish a suitable

---

Address reprint requests to E. R. Meinders, Delft University of Technology, Applied Physics Department, Heat Transfer Section, Lorentzweg 1, P.O. Box 5046, 2600 GA Delft, The Netherlands.

Received 10 March 1996; accepted 15 October 1996

Int. J. Heat and Fluid Flow 18: 152–159, 1997

655 Avenue of the Americas, New York, NY 10010

0142-727X/97/$17.00
PII S0142-727X(96)00139-9

environment for the in situ calibration. The ratio of the channel width to the cube dimension was 50/15 = 3.3. Free-stream velocities ranged between 1 and 6 m/s.

The measurement elements consist of an internal copper cubical core covered by a thin epoxy layer. A schematic drawing of a composed element is shown in Figure 2. Heat is generated in the copper core of the element by a dissipating resistance wire. The temperature decay across the copper core is negligible compared to the expoxy layer because of the high thermal conductivity of copper as compared to that of epoxy. This implies an almost uniform copper temperature (< 0.05°C), even for relatively high fluxes, which can easily be measured with a thermocouple. The outer surface temperature distribution of the epoxy layer was determined with infrared thermography. A simple one-dimensional (1-D) computation from the temperature difference between the inner and outer surface of the epoxy layer was unreliable due to strong 3-D effects. For that reason, the temperature distribution in the epoxy layer was calculated numerically by solving the 3-D conduction problem with appropriate boundary conditions, and the lateral effects were taken into account in determining the local heat fluxes at the element surface. The local equilibrium of heat fluxes at the surface finally results in a local convective heat flux ϕ''_{conv}:

$$\phi''_{\mathrm{conv}} = \phi''_{\mathrm{cond}|s} - \phi''_{\mathrm{rad}} \tag{1}$$

with $\phi''_{\mathrm{cond}|s}$ the conductive heat flux at surface and ϕ''_{rad} the radiative heat flux. The local adiabatic heat transfer coefficient h_{ad} reads (Meinders and van der Meer 1995b):

$$h_{\mathrm{ad}} = \frac{\phi''_{\mathrm{cond}|s} - \phi''_{\mathrm{rad}}}{T_{\mathrm{sur}} - T_{\mathrm{ad}}} \tag{2}$$

with T_{sur} and T_{ad} denoting, respectively, the surface and the adiabatic element temperature. The latter is defined as the temperature an element obtains when it is cut from power supply during the operation of all other elements (Moffat and Anderson 1990). Because the adiabatic element temperature can be examined locally, the adiabatic heat transfer coefficient is an appropriate parameter for describing the local heat transfer. With knowledge of the layer dimensions, thermal conductivity, and the temperature distribution in the epoxy layer, local conductive heat fluxes can be calculated (Meinders and van der Meer 1995b). Radiative heat flux was calculated from the surface temperature distribution, ambient temperatures (channel-walls), surface emissivity, and calculated view factors using the four-faces approach (Meinders and van der Meer 1995b). Heat losses through the mounting base and lead wires do not influence the obtained heat transfer coefficients. However, second-order effects are to be expected when heat losses by conduction via the lead wires and the baseplate preheat the upstream air flow.

Measurement procedure

Accurate measurements of the surface temperature of 3-D small objects placed in a channel is associated with a number of practical problems and uncertainties. The cubical protrusions are

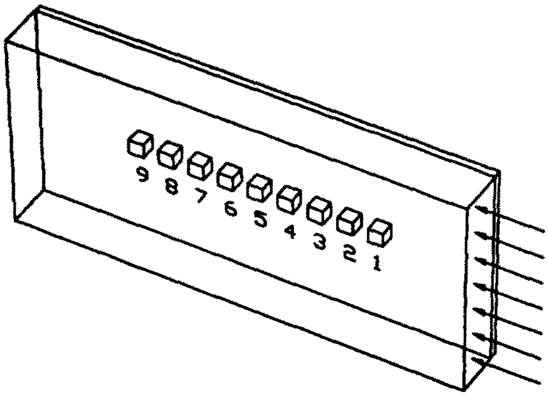

Figure 1 Schematic sketch of the test configuration

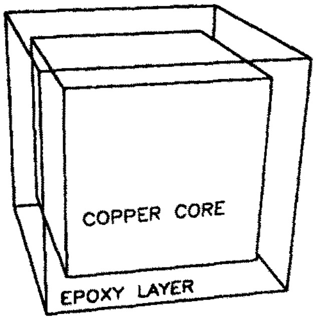

Figure 2 Schematic picture of the composed element

Notation

d	epoxy layer thickness, m
f_x, f_y	spatial frequencies, (1/m)
h_{ad},(htc)	adiabatic heat transfer coefficient, (W/m^{2}K)
i, j, k	indices
$i(x, y)$	original image
$h(x, y)$	optical transfer function
$m(x, y)$	measured image
n	normal direction
$n(x, y)$	noise image
$H(f_x, f_y)$	Fourier transform of $h(x, y)$
$I(f_x, f_y)$	Fourier transform of $i(x, y)$
$\hat{I}(f_x, f_y)$	Fourier transform of restored image
$M(f_x, f_y)$	Fourier transform of $m(x, y)$
$N(f_x, f_y)$	Fourier transform of $n(x, y)$
$W(f_x, f_y)$	reconstruction filter
N	grid size
T_{ad}	adiabatic component temperature, K
T_{amb}	ambient temperature, K
T_{co}	copper temperature, K
T_{sur}	surface temperature, K
U	free-stream velocity, (m/s)

Greek

ϵ	surface emissivity
λ	thermal conductivity, (W/mK)
σ	Stefan–Boltzmann constant, (W/m^{2}K^4)
$\phi''_{\mathrm{cond}|s}$	conductive heat flux at surface s, (W/m^2)
ϕ''_{conv}	convective heat flux, (W/m^2)
ϕ''_{rad}	radiative heat flux, (W/m^2)

located in a closed vertical channel, which requires the use of a window with transmissivity characteristics compatible with the optics of the infrared camera used. A shortwave infrared camera with optical transmission between 3 and 5 microns was used. The applied window (a foil with a uniform transmissivity of 0.84 for the entire wavelength region) meets this requirement.

Surface temperature distributions of the five faces of an element exposed to air flow are required to calculate the local convective heat fluxes. The four side faces of the cube, located perpendicular to the base-plate, are scanned under 45° angle. A schematic of this is presented as Figure 3. The consequence of a nonperpendicular scan direction is the decreasing spatial resolution. Enhanced radiation for infrared thermography is achieved by coating the surface with a high-emissivity paint. Experiments showed a uniform emissivity of 0.95 for scan angles up to approximately 55–60°. A scan angle of 45° ensures a sufficient spatial resolution (which is required to eliminate truncation errors when solving the Laplace equation) and a uniform emissivity.

Mapping

The total surface of the cubical element (except the bottom face) can be scanned within four projections: north-top (N-T), east-top (E-T), south-top (S-T) and west-top (W-T), as shown in Figure 4. Each face is divided into a certain number of surface cells ($N \times N$) according to the numerical grid, used to solve the Laplace equation.

Whenever the absolute location of a scanned face in the image is known, an averaged pixel value (intensity) can be calculated for each surface cell. These averaged intensities are transformed to surface temperatures by means of an appropriate calibration procedure, which is explained below. The number of surface cells is restricted by the spatial resolution of the infrared camera. With the selected object distance, focus length, optics, etc., a division of 30 × 30 seemed to be the optimum selection. With this division, the averaged number of pixels encountered per surface cell is approximately eight.

Grid element

Because the cube faces cover only a small part of the entire recorded image, location specification is necessary. In particular, the optic blur prevents correct identification of the exact position of the object in the image plane (see the image degradation section). This problem was solved by a grid element covered by a high-precision thermal grid. This grid element was made of copper with precisely located grooves filled with black paint. The high thermal conductivity of copper in contrast with the thermal resistance to air results in a uniform copper surface temperature. The pronounced emissivity differences between black paint ($\epsilon \approx 0.95$) and copper ($\epsilon \approx 0.3$) supplied an excellent contrast.

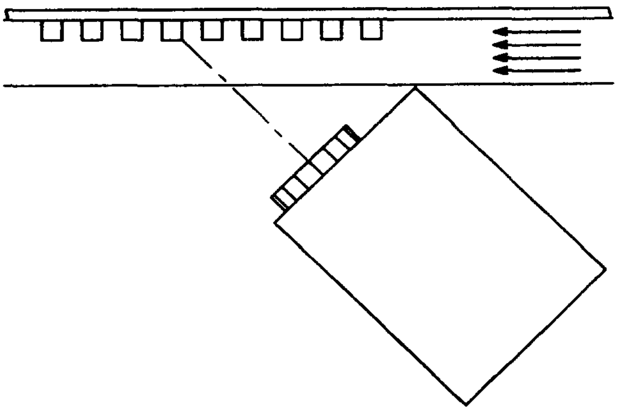

Figure 3 Experimental set-up of the infrared imaging system for scanning the east-top projection

Whenever the infrared camera is traversed with a traverse mechanism with a displacement accuracy of 0.1 mm, location identification of the grid element (farthest element location upstream in the array) can be applied to all other elements in the array. Of course, this requires accurate element positions relative to the grid element position. Optical aberrations and perspective functions can be determined with this grid element and applied to all other measurement elements.

In situ calibration

Infrared thermography is, in fact, based on the radiosity of a surface. Contributions from the environment to this radiosity (for example, reflections from hot neighbouring elements) are difficult to quantify and make an unambiguous temperature identification unrealiable without proper calibration. The concept is to substitute the measurement elements with an identical copper element (dimensions 15 × 15 × 15 mm, also coated with the same high-definition black paint) to incorporate environmental influences, transmissivities of used windows, reflections of neighbouring elements, etc. This in situ approach is valid provided that the situation during calibration is similar to the situation during performance of the experiments. The emitted radiation from that copper element is directly related to the actual copper temperature, and variation of the copper temperature results in the required calibration curves.

For each temperature level of this calibration element, infrared images of all faces (four projections) are recorded. With exactly the same procedure as described above, the different faces are divided in $N \times N$ surface cells, and the averaged pixel value is calculated. For each surface cell, a calibration curve remains, which relates the emitted intensity to the surface temperature. These curves are applicable to the measurement elements upstream resulting in surface temperatures.

Because both the calibration object and measurement elements are covered with the same black paint, an absolute value for the emissivity is not required. An absolute value is only desired for calculation of the net radiative heat flux in examination of the convective heat flux (see Equation 1).

Infrared system

The infrared camera used (Varioscan 1990) contains a scanning device that projects the incident radiation on one thermal cell (detector). Hysteresis, which is a significant problem for large scan-frequency cameras, is irrelevant, because we are considering a small scan frequency (2-Hz) camera. This was verified by recordings of perfect rotation symmetric hot objects (Meinders and van der Meer 1995a).

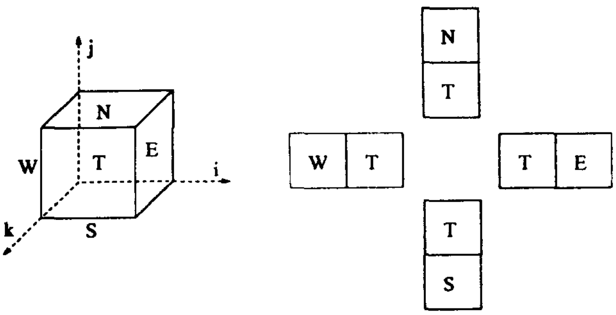

Figure 4 Schematic sketch of the four different projections

Because of the slow time response of the measurement elements, the relative small scan frequency of 2 Hz suffices. This time-independent behavior also permits the averaging of several recorded images for noise reduction.

The thermal resolution is determined by the smallest temperature range of the camera combined with the dynamic range of digitization. An 8-bit converter is used to digitize the received signal in 256 different energy levels (gray values). During performance of the experiments, a thermal resolution of at least 0.2°C was ensured.

Image degradation

Image degradation is the main source of temperature inaccuracy. If only the thermal value of individual pixel points is altered, degradation can be caused by noise introduced by the detector itself. This noise level was determined experimentally for several different situations and corresponds to temperatures of 0.10–0.12°C.

Spatial image degradation is a consequence of optical diffraction and aberration blur (for example, defocussing of the object). Spatial averaging over the instantaneous projected area is also classified as a possible cause of spatial image degradation (Rosenfeld and Kak 1982). Spatial degradation becomes more critical for small objects. Reconstruction techniques are required whenever the spatial degradation significantly affects the absolute accuracy of the temperature readings.

Because this degradation is caused by the optical system, a unique correlation can be assumed between the original, undistorted image and the measured, distorted image. In general, the relation between the distorted image $m(x,y)$ and the original image $i(x,y)$ can be expressed in the spatial domain as a convolution product (Mullikin et al. 1994; Bougeard et al. 1995):

$$m(x,y) = h(x,y) * i(x,y) + n(x,y) \tag{3}$$

where $h(x,y)$ is defined as the two-dimensional (2-D) transfer function, known better as the point spread function (PSF). It indicates the power distribution in the image plane due to a point source in the object plane. The contribution $n(x,y)$ represents random noise in the image plane. Fourier transformation of this convolution product results in an ordinary product:

$$M(f_x,f_y) = H(f_x,f_y)I(f_x,f_y) + N(f_x,f_y) \tag{4}$$

with $H(f_x,f_y)$ the optical transfer function (OTF) in spatial frequencies f_x and f_y. The modulus of this complex function is better known as the modulation transfer function (MTF). The blurred image can be restored with a reconstruction filter $\mathrm{W}(f_x,f_y)$ yielding the restored image $\hat{I}(f_x,f_y)$:

$$\hat{I}(f_x,f_y) = \mathrm{W}(f_x,f_y)M(f_x,f_y) \tag{5}$$

The Wiener filter is a suitable reconstruction filter that uses the two-dimension (2-D) OTF and the noise characteristics of the image, yielding an image with an acceptable noise level (Rosenfeld and Kak 1982).

The 2-D OTF was constructed from one-dimensional (1-D) edge transfer functions measured with a perfect thermal edge for different scan directions. This edge was created with a large copper plate covered with two significantly different emissivities. Differences in emissivities result in different emitted intensities. For a detailed discussion on the measurement techniques and method to determine this OTF, the reader is referred to Meinders et al. (1996).

The calibration method developed partially corrects for this spatial image degradation provided that similar operational conditions during calibration and measurements are ensured. Although this calibration method supplies thermal readings within an accuracy of 0.5–1.0°C, image reconstruction techniques are required to improve the accuracy of temperature measurements up to 0.3–0.4°C.

Accuracy of experimental results

The experimental method is evaluated with the standard single-sample uncertainty analysis recommended by Moffat (1988). The 1-D approximation of the conductive heat flux at the surface can be used to estimate its contribution to the total uncertainty in h_{ad} (W/m^{2}K).

$$\phi''_{\mathrm{cond}|s} = \lambda \left.\frac{\partial T}{\partial n}\right|_s = \lambda \frac{(T_{\mathrm{co}} - T_{\mathrm{sur}})}{d} \tag{6}$$

with T_{co} (°C) the copper temperature, T_{sur} (°C) the surface temperature, λ (W/mK) the thermal conductivity of the epoxy layer and $d(m)$ the epoxy layer thickness. The radiative heat flux is also simplified in order to calculate the uncertainty in the radiative heat flux. If no distinction is made between the base plate, the neighbouring cube and the remaining part of the environment (this simplification is only adopted to calculate the experimental uncertainty), the radiative heat flux can be assumed as:

$$\phi''_{\mathrm{rad}} = \epsilon\sigma(T^4_{\mathrm{sur}} - T^4_{\mathrm{amb}}) \tag{7}$$

where ϵ is the surface emissivity, σ the Stefan–Boltzmann constant ($= 5.670\ 10^{-8}$ W/m^{2}K^4) and T_{sur} (°C) and T_{amb} (°C) are the surface and ambient (channel walls) temperatures, respectively. In reality, the neighbouring element and the base plate do have a higher temperature than the ambient that is incorporated in the four faces approach used as discussed in Meinders and van der Meer (1995b). The resulting uncertainty in h_{ad} becomes:

$$\begin{aligned}(\delta h_{\mathrm{ad}})^2 = {} & \left(\frac{\left.\frac{\partial T}{\partial n}\right|_s}{(T_{\mathrm{sur}} - T_{\mathrm{ad}})}\right)^2 (\delta\lambda)^2 + \left(\frac{\lambda}{d(T_{\mathrm{sur}} - T_{\mathrm{ad}})}\right)^2 (\delta T_{\mathrm{co}})^2 \\ & + \left(\frac{4\epsilon\sigma T^3_{\mathrm{amb}}}{T_{\mathrm{sur}} - T_{\mathrm{ad}}}\right)^2 (\delta T_{\mathrm{amb}})^2 + \left(\frac{h_{\mathrm{ad}}}{T_{\mathrm{sur}} - T_{\mathrm{ad}}}\right)^2 (\delta T_{\mathrm{ad}})^2 \\ & + \left(\frac{\lambda(T_{\mathrm{co}} - T_{\mathrm{sur}})}{d^2(T_{\mathrm{sur}} - T_{\mathrm{ad}})}\right)^2 (\delta d)^2 + \left(\frac{\sigma(T^4_{\mathrm{sur}} - T^4_{\mathrm{amb}})}{T_{\mathrm{sur}} - T_{\mathrm{ad}}}\right)^2 (\delta\epsilon)^2 \\ & + \left(\frac{4\epsilon\sigma T^3_{\mathrm{sur}} + \lambda/d + h_{\mathrm{ad}}}{T_{\mathrm{sur}} - T_{\mathrm{ad}}}\right)^2 (\delta T_{\mathrm{sur}})^2\end{aligned} \tag{8}$$

The material constants λ and ϵ are determined experimentally. Locally, at the surface of an element, the emissivity can deviate because of differences in layer thickness of the black paint used. The thermal conductivity of the epoxy can also deviate because of anisotropic structures and/or internal stresses (caused, for example, by thermal expansion). Sensitivity studies proved that these uncertainties, estimated to be less than 2%, do not contribute significantly to the total error in the heat transfer coefficient.

The total error in the calculated temperature gradient at the surface $\partial T/\partial n|_s$ consists of a negligible numerical error (truncation error, because the Laplace equation is solved for the epoxy layer) and an experimental uncertainty.

The epoxy layer was carefully created with an imprecision in the thickness of less than 1% with deviations in thickness within 0.01 mm. The thermal expansion of the epoxy layer causes a relative increase in thickness of less than 0.6%. The internal copper temperature is measured with a thermocouple with an accuracy of 0.1°C after appropriate calibration. The uncertainty of 0.5°C in the ambient and adiabatic reference temperatures is not significantly affecting the total error in the heat transfer coefficient.

The major contribution to the inaccuracy in the adiabatic heat transfer coefficient comes from the surface temperatures of the elements. After application of the reconstruction technique, temperature readings for the middle region of the different faces are accurate within 0.3–0.4°C. However, the accuracy of the temperature at the edges is approximately 0.5–0.6°C.

A cumulative inaccuracy in the adiabatic heat transfer coefficient is between 5 and 10% (Meinders and van der Meer (1995b).

Validation of the temperature measurements

Liquid crystals, substances with the properties of both a liquid and crystalline state, are used to validate the surface temperature measurements performed with the infrared camera. For a detailed discussion of the different properties and possible applications, the reference is made to Moffat (1990) and Baughn (1994).

In this particular investigation, encapsulated cholesteric liquid crystals are used. The molecular ordering of these liquid crystals changes under the influence of temperature. This reversible change in molecular structure causes wavelength-selective reflection of the incident light. The unambiguous relation between the temperature and reflected light enables the observer to identify surface temperatures. The liquid crystals are encapsulated to protect them from atmospheric contamination in order to improve the stability.

A liquid crystal is characterized by its event temperature and the temperature range in which the crystal changes from colorless to red, green, blue, and back to colorless. For the present application, crystals were selected with narrow color-play bandwidths of approximately 2°C and event temperatures at, respectively, 47.5, 55.0, 60.0, 65.0, and 73.0°C (Parsley 1987). These microencapsulated liquid crystals were mixed to achieve a coating with multiple color ranges.

Color interpretation by the human eye is very subjective; therefore, we decided to consider only the five crossings between green and red (1 per event), because these color changes are very sharp and provide an objective interpretation. A 10-mm thick copper plate was used to calibrate the liquid crystals. A temperature difference across the plate was maintained by means of two heat exchangers. The resulting 1-D almost linear temperature decay was monitored with 29 thermocouples distributed over the plate width. These temperature readings were accurate within 0.1°C. The copper plate was painted with the liquid crystal mixture. The color patterns were photographed, and from these pictures, temperatures corresponding to the crossings between red and green were determined with an accuracy of 0.3–0.4°C. For the five subsequent liquid crystals, these temperatures are, respectively, 47.5, 55.8, 60.5, 65.2, and 72.8°C.

The surface of the fifth cubical element in the array was painted with the same mixture of liquid crystals. The color patterns were photographed, and at the crossings between red and green, the corresponding surface temperatures were attributed. These experiments were performed for the free-stream velocity of 5.1 m/s. The liquid crystal results are shown in Figures 5 and 6 together with the infrared temperature measurements without application of the image reconstruction technique. The cross sections, shown respectively, perpendicular and parallel to the base plate, are at centerline of the cube.

The differences between these liquid crystal and infrared temperature readings are caused by the spatial image degradation of the infrared camera used. Areas of sharp gradients are flattened. This flattening results in too low a temperature reading for certain areas (when an edge borders the ambient temperature) and sometimes in too high a temperature reading.

Figures 7 and 8 compare the liquid crystal experiments and infrared temperature measurements after application of the reconstruction technique. The uncertainty in temperature readings for both techniques is approximately 0.3–0.4°C. When a small uncertainty for the position is accounted for, results from the two independent measurement techniques are in excellent agreement.

Local convective heat transfer and flow pattern

Local convective heat transfer results are discussed for a free-stream velocity of 5.1 m/s. The cubical elements are adjusted at an internal copper temperature of 75.0°C. The air temperature at inlet was set by thermostat to 21.0°C.

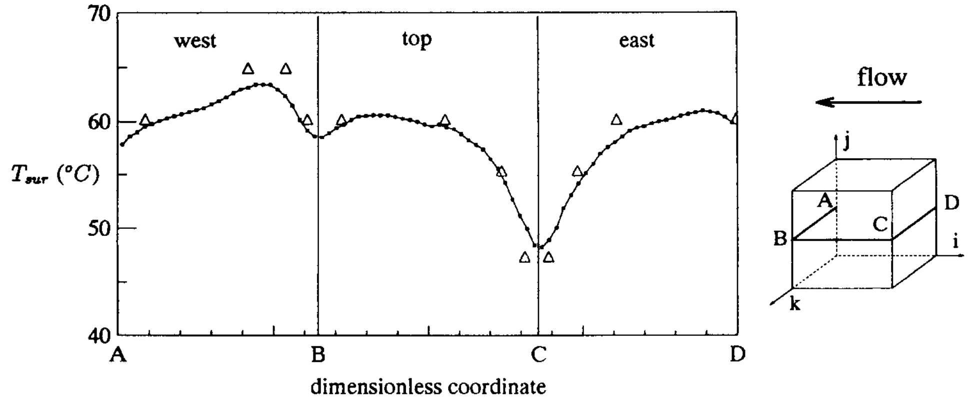

Figure 5 Comparison of surface temperature measurements between liquid crystal thermography (large △) and unreconstructed infrared results (small □) for a free-stream velocity of 5.1 m/s. The cross section ABCD is perpendicular to the baseplate

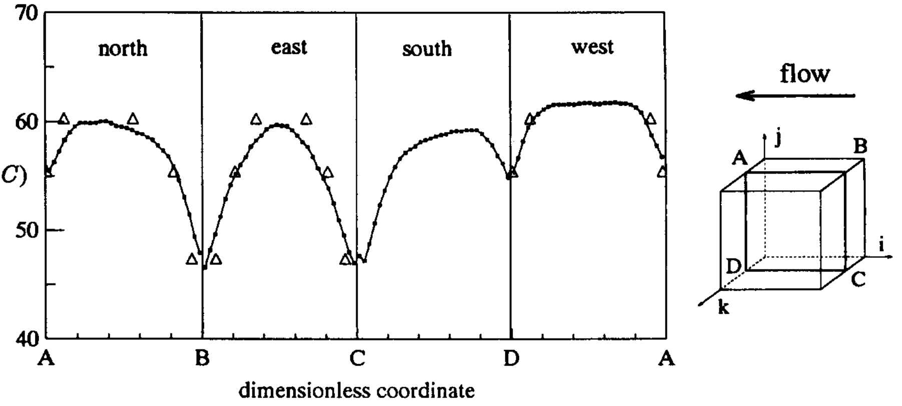

Figure 6 Comparison of the surface temperature measurements between liquid crystal thermography (large △) and unreconstructed infrared results (small □) for a free-stream velocity of 5.1 m/s. The cross section ABCDA is parallel to the baseplate.

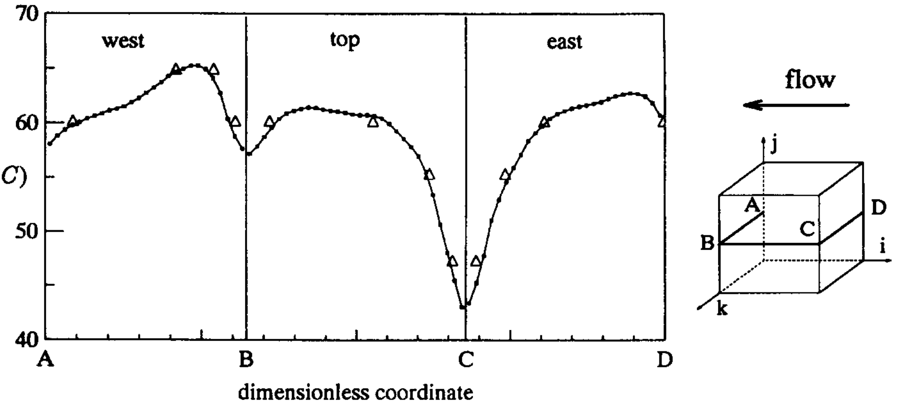

Figure 7 Comparison of surface temperature measurements between liquid crystal thermography (large △) and infrared results after application of the reconstruction technique (small □) for a free-stream velocity of 5.1 m/s. The cross section ABCD is perpendicular to the baseplate

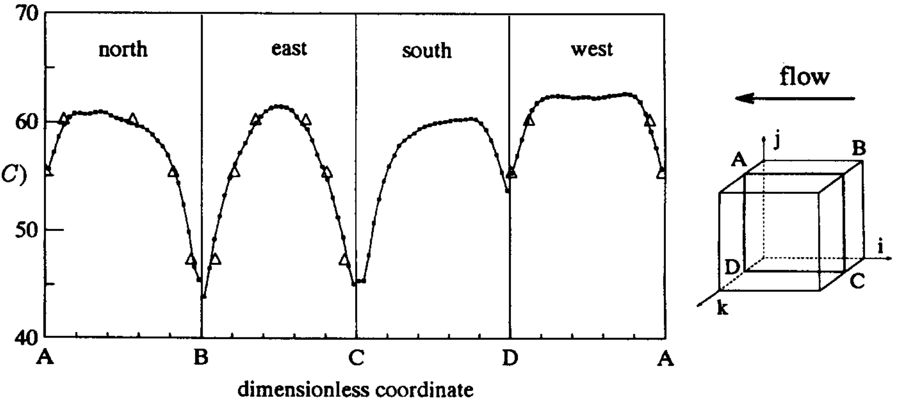

Figure 8 Comparison of surface temperature measurements between liquid crystal thermography (large △) and infared results after application of the reconstruction technique (small □) for a free-stream velocity of 5.1 m/s. The cross section ABCDA is parallel to the baseplate.

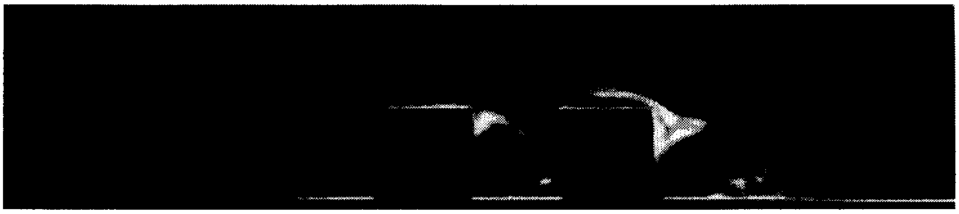

Figure 9 Smoke visualization of the flow patterns around an array of cubic elements at a plane perpendicular to the baseplate for a free-stream velocity of 1.2 m/s

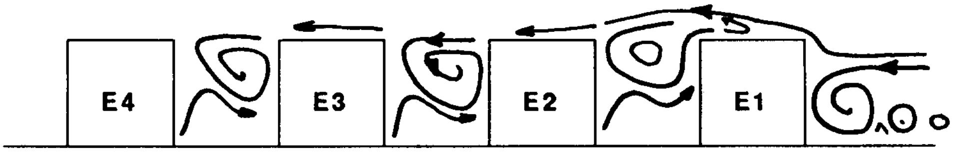

Figure 10 Schematic sketch of the flow patterns around an array of cubic elements at a plane perpendicular to the baseplate

Smoke visualization is used to characterize the flow around the cubical protrusions in the packed array. A laser sheet, which is created by a rotating mirror (polygon) and a coherent light beam (laser), is used for plane illumination. An instantaneous image of the flow patterns at the centreline of an array of cubical elements is shown in Figure 9. The plane of view is perpendicular to the base plate.

Flow visualizations were performed for free-stream velocities between 1 and 6 m/s. Because the instantaneous recordings of the flow structures are difficult to interpret, schematical sketches were constructed from the recorded images, corresponding to the velocity range 1–6 m/s.

Figure 10 is a schematic sketch of the flow patterns in a plane perpendicular to the base plate. The most pronounced feature that emerges from Figure 10 is the horseshoe vortex, which is induced at the front face of the first element and wraps around the base region. This phenomenon was observed by several researchers for a single element exposed to air flow (Larousse et al. 1991; Hunt et al. 1978).

Strong recirculation areas appear in the region between subsequent elements. No significant differences in flow structures were observed after the fourth element.

The flow pattern in the plane parallel to the base plate at half cube-height is shown in Figure 11. The horseshoe vortex is attaching on the second cube at both side-faces. The section between subsequent elements shows two vortices that circulate in opposite directions. From the second cube, attached boundary-layer flow develops at both side-faces with the absence of recirculation zones.

Features of local convective heat transfer coefficients are discussed for the fifth element in the array. Because the influence of the induced-buoyancy flow caused by the temperature difference between the heated elements and the surrounding air is negligible as compared to that of the main stream, the situation is characterized only by forced-convection.

Figure 11 Schematic sketch of the flow patterns in the plane parallel to the mounting base at half cube-height

Local heat transfer coefficients are presented in Figure 12 along several cross sections (ABCDA) parallel to the base plate, where k is the distance from the base plate. Almost perfect symmetric patterns appear on the north (AB) and south (CD) face (the symmetry plane is indicated with dotted lines).

The fluid flows in attached boundary layers along the south and north face, which are characterized by a strong decay in convective heat transfer in the direction of the rear edge. The pronounced minimum at the east face is caused by strong vortices between the two neighbouring elements, which circulate in the opposite direction, as shown in the above schematic sketches. The heat transfer at the west face is dominated by the recirculating flow in the region between subsequent elements. The convective heat transfer at the top face, shown in Figure 13, is also dominated by boundary-layer flow, which causes a decay in h_{ad} in the downstream direction.

Conclusions

The present paper focuses on the experimental techniques and methods for measuring local convective heat transfer from an array of a cubical protruding elements in a vertical channel flow. The findings can be summarized as follows.

1. An experimental method is presented to determine the local convective heat transfer from small cubical protrusions.
2. The surface temperature distribution of the elements, required to calculate the local convective heat transfer, was measured with an infrared system. An appropriate in situ calibration procedure was developed to relate the emitted radiosity to the actual surface temperature. Spatial image degradation seemed to be the main cause of temperature inaccuracy. Accurate temperature measurements were achieved by processing the infrared images with a Wiener reconstruction filter.
3. Liquid crystal thermography was used as second independent technique to measure the surface temperatures at certain distinct locations. Excellent agreement was observed between these liquid crystal results and the surface temperature distribution obtained from infrared thermography after application of the Wiener reconstruction technique.
4. A pronounced variation in the local heat transfer coefficients was observed, as a consequence of complex flow structures around the elements, with flow separation and reattachment.
5. The flow patterns, obtained with visualisation techniques, facilitated the interpretation of the variation of the local heat transfer coefficients.

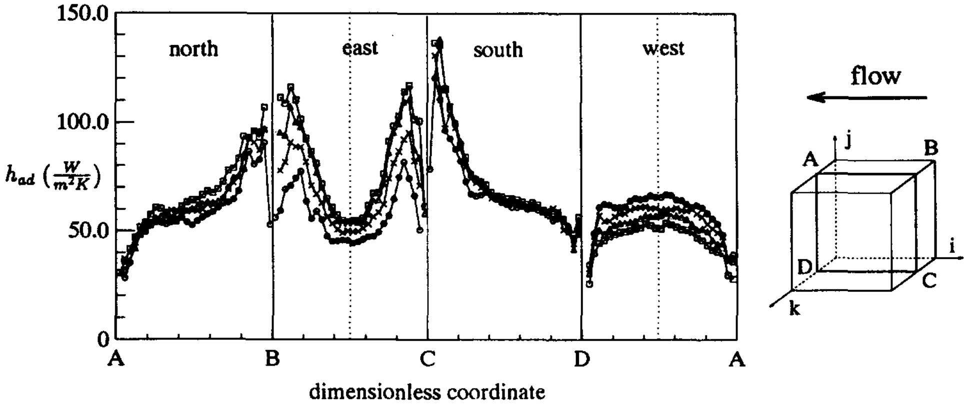

Figure 12 Adiabatic heat transfer coefficients for the fifth element and cross sections parallel to the baseplate for different distances from the baseplate: O 3.5 mm, × 5 mm, △ 6.5 mm and □ 7.5 mm

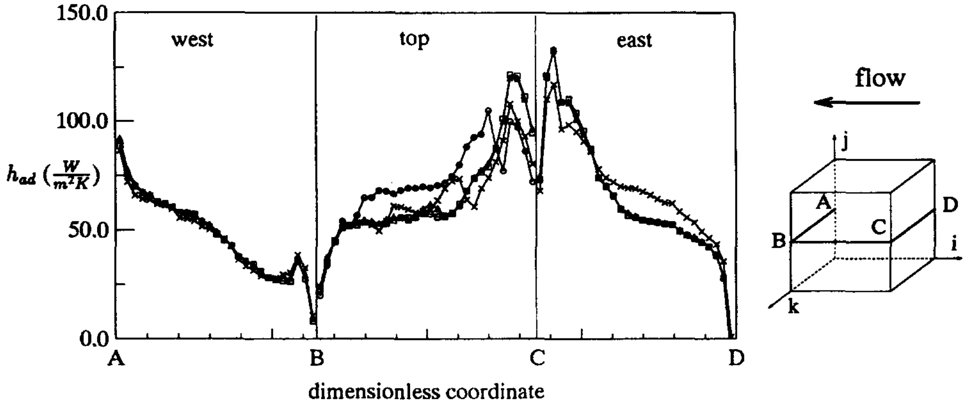

Figure 13 Adiabatic heat transfer coefficients for the fifth element for cross sections perpendicular to the base: O 2.5 mm, × 4.5 mm, △ 6.5 mm and □ 7.5 mm

References

Baughn, J. W. 1994. Liquid crystal methods for studying turbulent heat transfer. *Proc. Int. Symposium on Turbulence, Heat and Mass Transfer*, Lisbon, Portugal

Bougeard, D., Vermeulen, J. P. and Baudoin, B. 1995. Mesure du champ de temperature sur une ailette d'echangeur par thermographie infrarouge. *Révue Generale de Thermique*, **34**, 325–334

Hunt, J. C. R., Abell, C. J., Peterka, J. A. and Woo, H. 1978. Kinematical studies of the flows around free or surface-mounted obstacles; Applying topology to flow visualisations. *J. Fluid Mech.* **86**, 179–200

Larousse, A., Martinuzzi, R. and Tropea, C. 1991. Flow around surface-mounted, three-dimensional obstacles. *Proc. 8th Symposium Turbulent Shear Flows*, Munich, Germany, **1**, 14-4-1–14-4-6

Meinders, E. R. and Meer, T. H. van der 1995a. The performance of the VARIOSCAN Infrared system, Internal rep. WT.95.5, Delft University of Technology, Delft, The Netherlands

Meinders, E. R. and Meer, T. H. van der 1995b. Local convective heat transfer from an array of 9 cubical components in vertical channel flow. Internal rep. WT.95.6, Delft University of Technology, Delft, The Netherlands

Meinders, E. R., Kempen, G. M. P. van, Meer, T. H. van der and Vliet, L. J. van 1996. Infrared image reconstruction to improve the accuracy of surface temperature measurements of small objects. to be published

Moffat, R. J. and Anderson, A. M. 1990. Applying heat transfer coefficient data to electronics cooling. *J Heat Transfer*, **112**, 882–890

Moffat, R. J. 1988. Describing the uncertainties in experimental results. *Exp. Therm. Fluid Sci.*, **1**, 3–17

Moffat, R. J. 1990. Experimental heat transfer. *Proc. 9th Int. Heat Transfer Conference*, Jerusalem, Israel, **1**, 187–205

Mullikin, J. C., Vliet, L. J. van, Netten, H., Boddeke, F. R., Feltz, G., van der and Young, I. T. 1994. Methods for CCD camera characterization. *SPIE—The International Society for Optical Engineering*, **2173**, 73–84

Parsley, M. 1987. An Introduction to Thermochromic Liquid Crystals. Hallcrest, Glenview, IL, USA

Rosenfeld, A. and Kak, A. C. 1982. Digital image processing, 2nd ed. Academic, Orlando, FL, USA

Varioscan. 1990. Handbook, Jenoptik Technology, Jena, Germany